Journal of Solid State Electrochemistry
https://doi.org/10.1007/s10008-019-04315-4

ORIGINAL PAPER

Hydrothermal microwave-assisted synthesis of Li_3VO_4 as an anode for lithium-ion battery

G. S. Zakharova[1] · E. Thauer[2] · S. A. Wegener[2] · J.-H. Nölke[2] · Q. Zhu[3] · R. Klingeler[2,4]

Received: 6 March 2019 / Revised: 3 May 2019 / Accepted: 3 June 2019

Abstract

Li_3VO_4 with various morphologies has been synthesized by a microwave-assisted hydrothermal method. It is shown that the crystal size and morphology of Li_3VO_4 are determined by the type of solvent in the reaction solution and possible reasons of the solvent-type effect are discussed. Electrochemical studies of as-prepared Li_3VO_4 as anode materials for Li-ion batteries demonstrate a clear influence of the materials' morphology and surface properties on the electrochemical performance. Li_3VO_4 nanocrystals with a porous structure exhibit an enhanced electrochemical activity with an initial discharge capacity of 163 mAh g^{-1}.

Keywords Li_3VO_4 · Hydrothermal synthesis · Anode material · Lithium-ion batteries

Introduction

Lithium-ion rechargeable batteries have high current and power densities compared with other rechargeable batteries. The major challenges in designing next-generation lithium-ion batteries (LIB) include the need to increase their energy density, cycling life, and charge/discharge rate capability. This demands the design of improved electrode materials with favored properties, e.g., fast Li-ion diffusion and small volume changes upon electrochemical cycling [1]. In this respect, among the different reaction mechanisms, intercalation-type anodes are particularly promising [2, 3]. The commercially widely used graphite features a high theoretical capacity of 372 $mAhg^{-1}$ [4, 5]. However, it exhibits a low voltage plateau (below 0.3 V vs. Li/Li^+) near to the potential to that of deposition of Li metal which involves the risk of dendrite formation [6]. Alternative materials LIBs are $Li_4Ti_5O_{12}$ and TiO_2. In particular, the spinel $Li_4Ti_5O_{12}$ is used in niche applications as it can accommodate three Li-ions with a, however, low theoretical specific capacity of 175 $mAhg^{-1}$ at a flat potential of 1.55 V [7, 8]. TiO_2 demonstrates double theoretical specific capacity (335 $mAhg^{-1}$ at $x = 1$ in Li_xTiO_2) and high Li insertion potential (1.5–1.8 V vs. Li/Li^+) [9]. However, the maximum value of Li insertion is limited to $x = 0.5$, corresponding to the theoretical capacity of 167.5 $mAhg^{-1}$ [10]. Additionally, this material has low electrical conductivity and poor cycling performance. Good electrochemical performance was reported for elongated TiO_2 nanostructures such as rods or tubes [11, 12]. Due to high aspect ratio and porous morphology, TiO_2 nanostructures allow efficient transport of lithium ions and a high charge/discharge capacity (about 250 $mAhg^{-1}$).

Recently, lithium orthovanadate, Li_3VO_4, has been suggested as another promising intercalation-type anode material for lithium-ion batteries [13–19]. In comparison with graphite, $Li_4Ti_5O_{12}$, and TiO_2, lithium orthovanadate could be intercalated by Li-ions in the voltage range of 0.2–1.0 V (vs. Li/Li^+). Its high working voltage offers a save operating potential and allows to effectively avoid the deposition of lithium metal on the electrode. In addition, it demonstrates a large theoretical reversible specific capacity comparable to that of graphite (394 $mAhg^{-1}$) corresponding to $x = 2$ in $Li_{3+x}VO_4$. Low

Electronic supplementary material The online version of this article (https://doi.org/10.1007/s10008-019-04315-4) contains supplementary material, which is available to authorized users.

✉ G. S. Zakharova
gszakharova@mail.ru

[1] Institute of Solid State Chemistry, Ural Division, Russian Academy of Sciences, Yekaterinburg, Russia

[2] Kirchhoff Institute of Physics, Heidelberg University, Heidelberg, Germany

[3] School of Material Science and Engineering, Wuhan University of Technology, Wuhan, China

[4] Centre for Advanced Materials, Heidelberg University, Heidelberg, Germany

Published online: 17 June 2019

and safe voltage combined with a large specific capacity permit to claim that Li_3VO_4 might play a promising role as a new insertion anode for LIB.

There are two known Li_3VO_4 polymorphs: the low-temperature β-form and the high-temperature γ-form. Its crystal structure belongs to the Li_3PO_4-type which is composed of a 3D network of corner-sharing LiO_4 and VO_4 tetrahedrons (Fig. 1). The empty sites of the crystalline framework generate straight channels along the *a*- and *c*-axes, and zigzag channels along the *b*-axis, both of which providing potential intercalation paths for Li-ions.

Various methods have been attempted to synthesize Li_3VO_4, including solid-state reaction [14, 20, 21], hydrothermal [22–24], aerosol spray [25], sol-gel [26, 27], precipitation [20], and self-template [28] methods. Solid-state synthesis and precipitation are the most conventional and widely used chemical syntheses. Nevertheless, they lead to broad particle size distributions of the final product. Besides, it is hard to prevent the agglomeration of the primary nanoparticles, which may cause poor electrochemical performance. Whereas, sol-gel and conventional hydrothermal methods can promote precursors to achieve mixing and homogenizing up to the nanometer level. Both procedures, however, usually require a long and time-consuming sintering process. Similarly, as the aerosol spray method is also costly in terms of time and requires sophisticated equipment, it is not advantageous for large-scale production. Compared with conventional methods, hydrothermal microwave-assisted synthesis is quite faster, simpler, and more energy-efficient providing the production of the final product with a smaller particle size and improving its electrochemical performance [29].

In this paper, the hydrothermal microwave-assisted route is introduced to synthesize Li_3VO_4. The study is focused on the results of the structure, morphology, and electrochemical performance of Li_3VO_4.

Experimental

The starting materials used in the experiment were of analytical grade and purchased from Sigma–Aldrich. In a typical procedure, 0.234 g NH_4VO_3 and 0.252 g $LiOH{\cdot}H_2O$ (the molar ration of NH_4VO_3 to $LiOH{\cdot}H_2O$ = 1:3) were dissolved in 30 ml distilled water. After stirring for 20 min, the clear solution was poured into a sealed glass vial and then transferred into a microwave reactor (Monowave 300, Anton Paar). On a ramping time of 10 min, the vial was heated at 180 °C, held at this temperature for 20 min, and cooled by compressed air up to 40 °C. The product was collected by centrifugation and washed with deionized water several times. The as-prepared material is labeled as Li_3VO_4-W. For the purpose of comparison, Li_3VO_4 was also prepared in an ethanol-assisted route using a volume ratio of C_2H_5OH to H_2O = 1:1. The resulting material is denoted as Li_3VO_4-E. To investigate the effect of pounding on the electrochemical activity, Li_3VO_4-E powder was grinded using a mortar for 15 min; this sample is labeled as Li_3VO_4-E(G).

The structure and morphology of the resulting product were characterized by X-ray powder diffraction (Shimadzu XRD-7000S, Cu K_α radiation, $\lambda = 1.540$ Å), ZEISS Leo 1530 scanning electron microscopy (SEM), and JEOL JEM 2100 *transmission electron microscopes* (TEM). The specific surface area and pore volume of the samples were measured by a surface area and porosity analyzer (Gemine VII, Micromeritics).

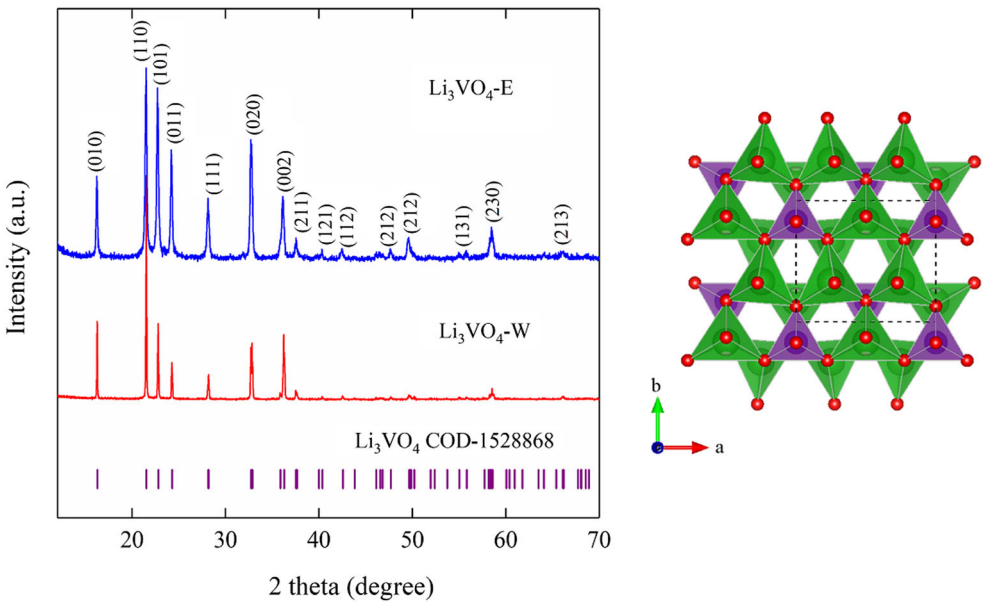

Fig. 1 XRD patterns of Li_3VO_4 synthesized in the presence of ethanol (blue line), in water without ethanol (red line), and the expected Bragg positions for the Li_3VO_4 structure (left). Crystal structure of Li_3VO_4 along (001) direction (right). Oxygen atoms are denoted by red balls, and LiO_4 and VO_4 tetrahedra are marked by green and violet color, respectively

Electrochemical studies were performed in Swagelok-type two electrode cells using a VMP3 potentiostat (Bio-Logic SAS) at 25 °C (see [30]). The working electrodes were prepared by mixing Li_3VO_4, carbon black (Timcal), and polyvinylidene fluoride binder (PVDF, Solvay Plastics) dissolved in N-methyl-2-pyrrolidone (NMP, Sigma–Aldrich) in a weight ratio of 75:20:5. In order to ensure a homogeneous distribution, the mixture was stirred for at least 12 h. Afterwards, most of the NMP was evaporated to obtain a spreadable slurry that was applied on circular Cu-meshes with a diameter of 10 mm. The electrodes were dried in a vacuum oven at 80 °C, mechanically pressed with 8 MPa, and then dried again. The loading density was about 2 mg cm^{-2}. As counter electrode, a lithium metal foil disk (Alfa Aesar) pressed on a nickel current collector was used. Both electrodes were separated by two layers of glass fiber separator (Whatman GF/D), which was soaked with 200 μl electrolyte (Merck Electrolyte LP30), a 1 M $LiPF_6$ salt solution in 1:1 ethylene carbonate (EC) and dimethyl carbonate (DMC). The cells were assembled in a glove box under an argon atmosphere ($O_2/H_2O < 5$ ppm).

Results and discussion

Lithium orthovanadate, Li_3VO_4, was synthesized by the following reaction:

$$3LiOH + NH_4VO_3 \rightarrow Li_3VO_4 + NH_3 + 2H_2O. \quad (1)$$

In Fig. 2, the XRD pattern of the material prepared using pure water as solvent (marked W) is shown in comparison to the one synthesized in the presence of ethanol (marked E). All diffraction peaks of the patterns can be indexed in the orthorhombic β-Li_3VO_4 phase with the space group $Pnm2_1$ according to the standard pattern of COD-1528868. Lattice parameters determined by means of full-profile analyses with the FullProf Suite are in a good agreement with reference data (Table S1). As shown in Fig. 1, Li_3VO_4-W exhibits sharper diffraction peaks which we associate to the larger crystal size in comparison with samples synthesized in the presence of ethanol. The crystallite sizes of the as-synthesized samples are calculated using Scherrer equation:

$$D = K\lambda/\Delta(2\theta)\cos\theta, \quad (2)$$

where D is the average grain size based on the particular reflecting crystal face (hkl) direction, K is a shape factor which can be approximated to 0.93, λ is the wavelength of the applied Cu Kα radiation, $\Delta(2\theta)$ is the full width at half-maximum of the diffraction peak, and θ is the Bragg angle. The analysis of the 110 and 101 peaks yields average crystallite sizes of 68 ± 5 nm for both Li_3VO_4-E and Li_3VO_4-E(G) samples. In contrast, Li_3VO_4-W is a bulk material with an average crystallite size of more than 100 nm which renders Scherrer's formula non-applicable. This indicates that the crystal size decreases with the addition of ethanol to the reactive system.

The influence of the solvent type on the morphology of the synthesized samples is further examined by SEM as illustrated in Fig. 2. As shown in Fig. 2a, Li_3VO_4-W which is hydrothermally synthesized with water as solvent mainly possesses irregular aggregates. Some particles exhibit a truncated tetragonal pyramid-like shape with sharp corners and well-defined edges of 1–4 μm in length. These particles show smooth surfaces. In the presence of ethanol as solvent in the reactive system, self-assembled hierarchical porous microspheres with a size of around 1 μm are formed (Fig. 2b). The surface of Li_3VO_4-E is very rough and consists of numerous flake-like nanoparticles which sizes range from 40 to 200 nm. Between these particles, the large holes are distinctly exhibited (Fig. 2c). Similar Li_3VO_4 particles of sphere-like shape have been also fabricated with the usage of ethanol as solvent under conventional hydrothermal conditions by other researchers [31]. As seen in Fig. 2d, grinding of Li_3VO_4-E yields breaking of the sphere-like particles and formation of weakly agglomerated of about 50–70-nm-sized nanocrystals (Li_3VO_4-E(G)). Note that according to Scherrer's analysis, it does not significantly affect the primary particles size but mainly affects agglomerates.

Additionally, TEM investigation was applied to further study the morphology of Li_3VO_4-E in detail. As shown in a low-magnification TEM image in Fig. 3a, the Li_3VO_4-E compounds are composed of sphere-like microparticles which size ranges from 0.9 to 1.5 μm. As seen, these particles show uneven surfaces with cavities. The high-resolution TEM (HRTEM) image of Li_3VO_4-E in Fig. 3b exhibits lattice fringes with spacing of 0.35 nm, which corresponds well with the (011) plane of the orthorhombic Li_3VO_4.

Our data highlight the crucial role of solvent in the synthesis process. The morphology of samples prepared using a mixture of water and ethanol as solvents significantly differs from that of Li_3VO_4 synthesized in H_2O only. It is known that the polarity and the saturated vapor pressure of the solvents during the hydrothermal (solvothermal) treatment are relevant solvent parameters which determine the morphology and size of the final product [32]. The polarity of the solvent is proportional to the dielectric constant, which for water and alcohol is 80.1 and 25.3 at 25 °C, respectively [33]. Chen et al. have determined the correlation between particle size and dielectric constant of alcohol/water solution [34]. There is a linear relationship between the reciprocal of particle size and the reciprocal of the dielectric constant for various kinds of alcohols which implies that the polarity of the solvents affects the nucleation rate and particle size of the prepared nanoparticles. In general, more polar solvents facilitate nucleation and tend to result in bigger particles according to the Ostwald ripening

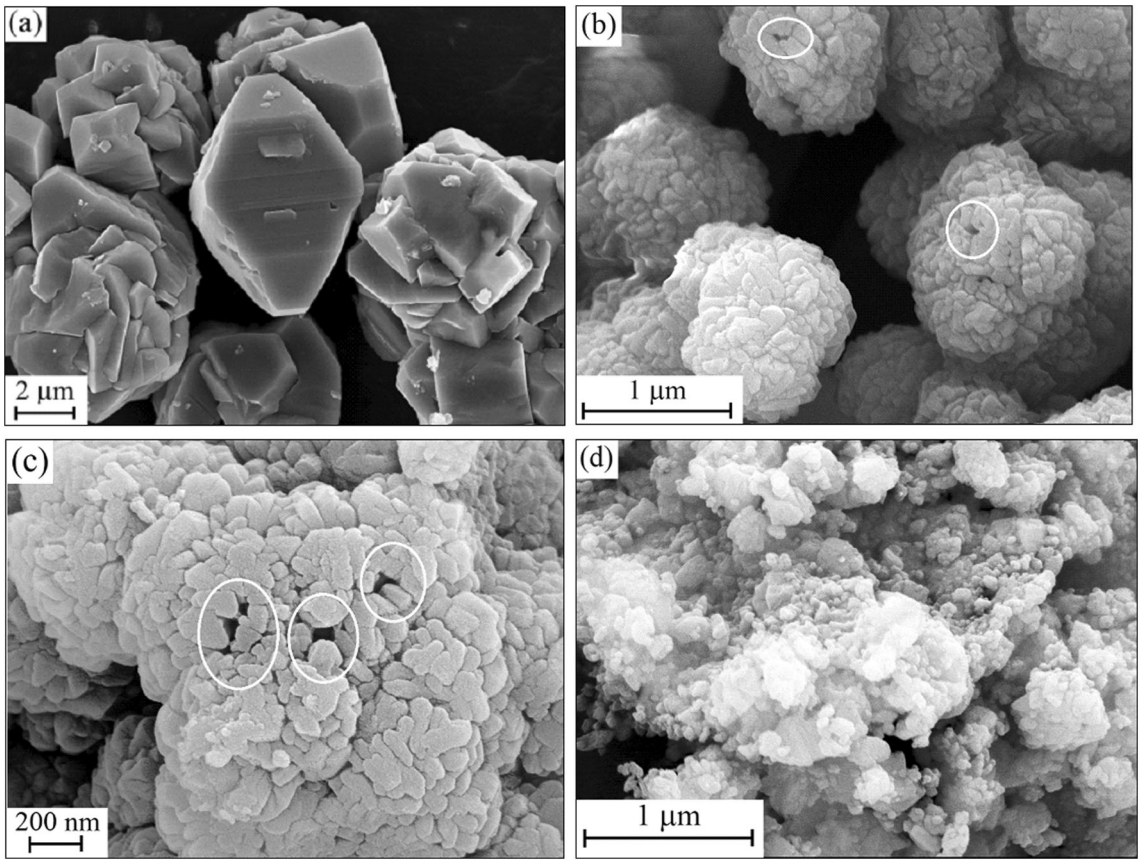

Fig. 2 SEM images of Li_3VO_4-W (**a**), Li_3VO_4-E at low (**b**) and high (**c**) magnifications, and Li_3VO_4-E(G) (**d**). Large holes in Li_3VO_4-E particles are shown by white circles

process [35]. The saturated vapor pressure influences not only the nucleation of the crystals but also the morphology of the materials since it is inversely proportional to the boiling point of the solvents [36]. For water and ethanol at ambient pressure, the boiling points of water and ethanol amount to 100 and 78.29 °C, respectively [33]. Accordingly, larger Li_3VO_4 crystals with faceted morphologies were obtained in water which possesses lower vapor pressure. This implies that the lower saturated vapor pressures assist more rapid growth of the Li_3VO_4 nuclei, resulting in larger particles. In contrast, the saturated vapor pressure of ethanol is high, so that growth of the Li_3VO_4 nuclei is limited, leading to the predominant nucleation of nanosized particles. Aggregation of these nanoparticles to the observed clusters and assemblies of various morphology takes place to reduce the overall surface area and thus to lower the surface energy of the compound.

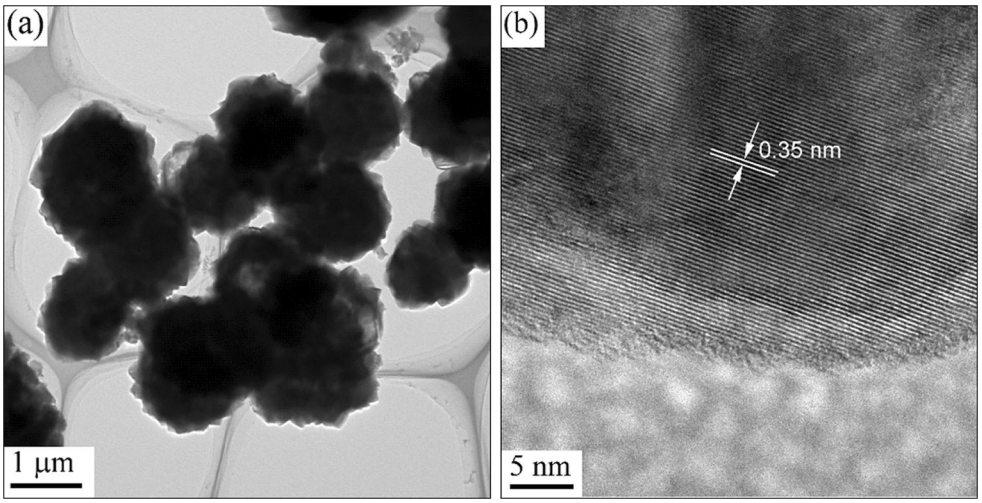

Fig. 3 (**a**) TEM and (**b**) HRTEM images of Li_3VO_4-E

In addition to size of primary and secondary particles, electrochemical activity of a material is influenced by surface properties such as specific surface area and pore size distribution. Both properties have been investigated on the Li_3VO_4 samples at hand by physisorption of nitrogen using the Brunauer–Emmett–Teller (BET) method. The specific surface area, average pore size, and total pore volumes for the samples are summarized in Table S1, indicating that the use of different solvents has substantial effects on the textural properties of the materials. The nitrogen adsorption–desorption isotherms of Li_3VO_4-W (data not shown) imply a very low surface area of roughly 0.02 $m^2\ g^{-1}$ as expected for a typical bulk material with a non-porous structure. The similar value of the specific surface was obtained by G. Yang et al. [22]. In contrast, application of ethanol as solvent during the hydrothermal treatment increases the specific surface area of the sample to 2.36 $m^2\ g^{-1}$. Additionally, grinding of Li_3VO_4-E further increases the BET surface area by nearly four times (8.91 $m^2\ g^{-1}$). According to the classification of IUPAC [37], sorption isotherms (Fig. 4a) obtained on Li_3VO_4-E prepared with ethanol as solvent feature a type IV behavior with a type H3 hysteresis, which is a characteristic for particles with rather uniform particle size distribution and a slit-shaped mesoporous structure. Analysis of the pore size distribution (Fig. 4b) shows that both Li_3VO_4-E and Li_3VO_4-E(G) samples exhibit a wide pore size distribution from 2 to more than 120 nm. Li_3VO_4-E mainly features mesopores which sizes are centered at around 11 and 17 nm. Grinding, which yields the abovementioned partial breaking of agglomerates, also affects the porosity: the pore-size distribution of Li_3VO_4-E(G) is rather broad and has two distinct maxima. One of which is associated with mesopores of about 5 nm. According to the literature, these pores may be attributed to the presence of interstices between the primary particles [38]. The larger pores (concentrated around ~ 36 nm) of Li_3VO_4-E(G) are supposed to result from aggregation of the nanosized crystals. To summarize, the obtained textural parameters show that use of ethanol as solvent and grinding of the final product yields increase of surface area and porosity which both may enhance applicability of the materials for electrodes in LIB.

In order to assess the effects of modified materials parameters on the electrochemical performance, Li_3VO_4-based electrodes have been investigated by means of cyclic voltammetry and galvanostatic cycling with potential limitation (GCPL) in the range 0.2–3.0 V. Figure 5 a shows the first, second, and tenth cycle of the cyclic voltammogram (CV) of Li_3VO_4-E recorded at a scan rate of 0.1 mV/s. The first reductive sweep shows a weak peak R_1 at 1.19 V and three pronounced ones at 0.67 V (R_2), 0.37 V (R_3), and at the lower limit 0.2 V (R_4). The peaks R_2 and R_3 can be assigned to intercalation of Li^+ into Li_3VO_4 [39]. During the first cycle, formation of the SEI contributes to the electrochemical activity in the same voltage range [23]. As of the second cycle, a shift of the peaks R_2 and R_3 to slightly higher potentials 0.82 V or rather 0.56 V is observable which is attributed to structural changes caused by an irreversible phase transformation during initial cycling [39, 40]. The first oxidative scan shows the main peak O_2 around 1.18 V, which corresponds to the delithiation of Li_3VO_4 [39], and a weak peak O_3 around 2.5 V. Upon further cycling, O_2 gets broader and the oxidation peak O_1 around 0.3 V shows up. The redox pair O_1/R_4 corresponds to the de−/lithiation processes related to carbon [41]. However, the underlying processes of the weak peaks R_1 and O_3 that are observed also by Ni et al. [23] remain unclear.

In order to investigate the cycling performance and rate capability of Li_3VO_4 with different morphologies, GCPL

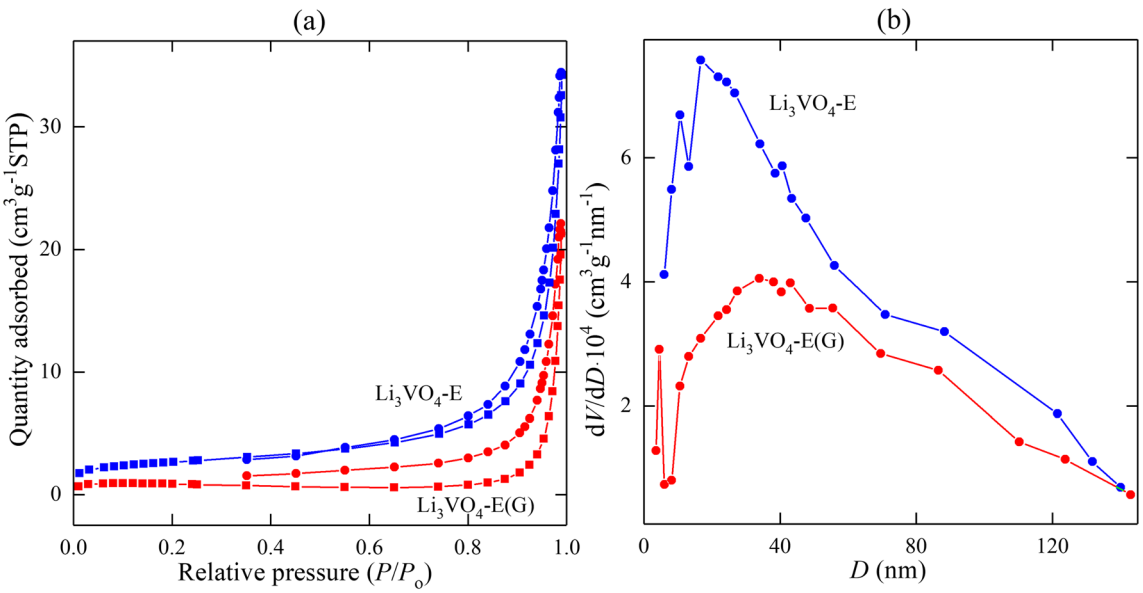

Fig. 4 (**a**) Nitrogen sorption isotherms and (**b**) corresponding pore size distribution curve of Li_3VO_4-E and Li_3VO_4-E(G) samples

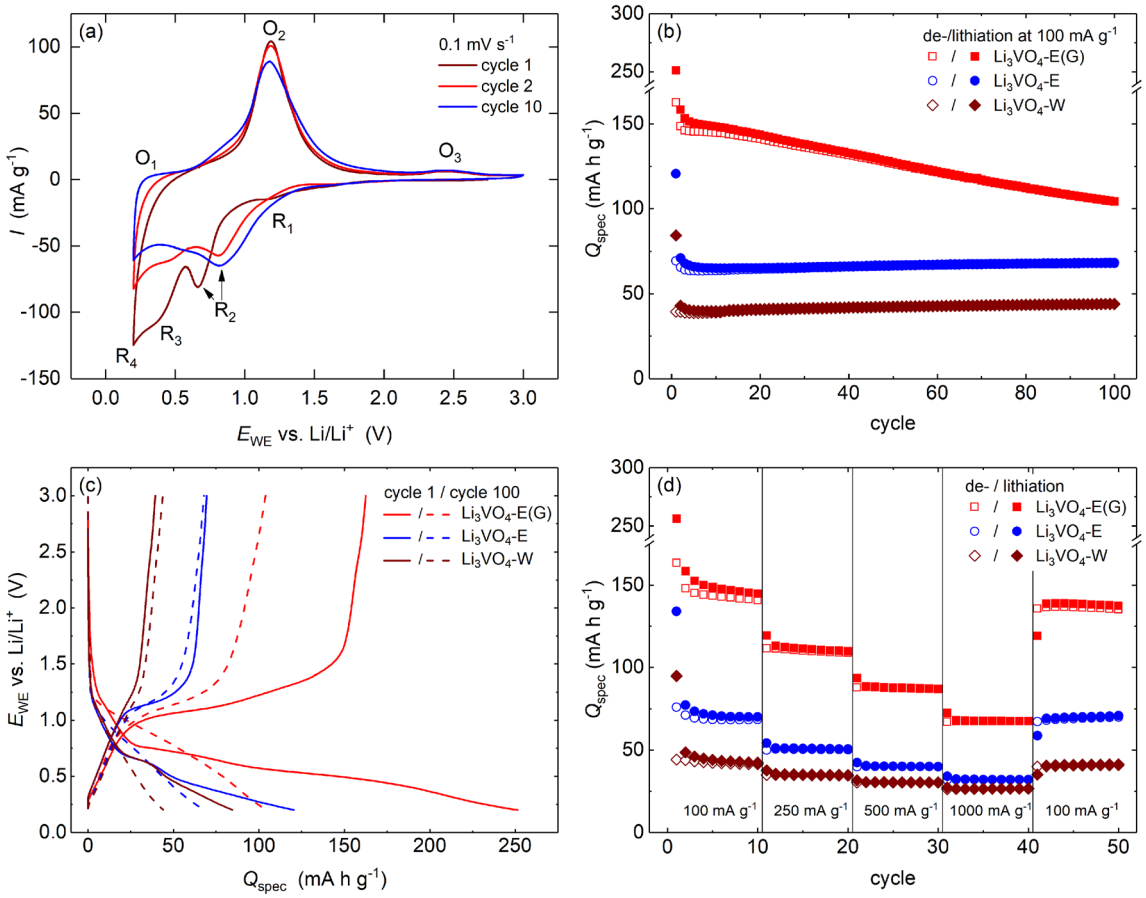

Fig. 5 (**a**) CV of Li_3VO_4-E studied at a scan rate of 0.1 mV s^{-1}. Specific charge/discharge capacities (**b**) and (**c**) potential profiles of the first and hundred cycles of Li_3VO_4-W, Li_3VO_4-E, and Li_3VO_4-E(G) for galvanostatic cycling at 100 mA g^{-1}. (**d**) Capability test with different cycling rates between 100 and 1000 mA g^{-1}

measurements have been performed. Figure 5 b shows the evolution of charge/discharge capacities during long-term measurements at a current density of 100 mA g^{-1} for 100 cycles. The belonging potential profiles in Fig. 5c exhibit plateaus corresponding to the peaks that are visible in the CV (Fig. 5a). For each sample, there is a large irreversible contribution in the first half cycle due to the SEI formation and structural changes [21, 39]. It is noticeable that the nanocrystals (Li_3VO_4-E(G)) reach the highest capacity over all cycles. In the first and the hundredth cycle, a charge capacity of 163 and 104 mAh g^{-1} is measured, respectively, while for the porous hierarchical microspheres (Li_3VO_4-E) just 69/68 mAh g^{-1} and for the bulk material with non-porous structure (Li_3VO_4-W) 39/44 mAh g^{-1} are reached. Comparing the samples that have been synthesized with and without ethanol shows that Li_3VO_4-E, which features more than 100 times larger surface, achieves about 60% higher capacity than Li_3VO_4-W. Grinding of sample Li_3VO_4-E results in a more than three times larger surface area and yields an increase of the capacity of around two times for Li_3VO_4-E(G). As expected, larger reaction surface leads to a higher electrochemical activity of Li_3VO_4 as on the one hand electrolyte diffusion is facilitated, and on the other hand, a large contact area with the conductive additive enables good electron transport pathway [22]. However, regarding the relative cycling stability, the grinded sample Li_3VO_4-E(G) delivers the least results with a discharge capacity loss of 36% between the first and hundredth cycle. In contrast, the other materials exhibit a more stable behavior. In case of Li_3VO_4-E, a small capacity loss of 1% and for Li_3VO_4-W even an increase of 13% is observable. The lower cycling stability of Li_3VO_4-E(G) may be attributed to huge charge depth yielding to structure damage caused by distortion and expansion upon cycling [21].

Furthermore, the rate capability of the different samples was studied at cycling rates between 100 and 1000 mA g^{-1}. The specific charge/discharge capacities are shown in Fig. 5d and the potential profiles in Fig. S1-S3. Again, the nanocrystals Li_3VO_4-E(G) show enhanced rate performance. Even at a high current density of 1000 mA g^{-1}, a discharge capacity of 67 mAh g^{-1} is still achieved, which is more than twice of that of the other materials. Moreover, it is observable that the capacity of Li_3VO_4-E(G), Li_3VO_4-E, and Li_3VO_4-W can regain to about 96%, 97%, and 95% when the current density returns to the initial value of 100 mA g^{-1}. Notably,

Table 1 Summary of the electrochemical performance of Li_3VO_4 electrodes prepared via different synthesis methods

Method	Current density 1 C ≈ 394 mA g^{-1} (mA g^{-1})/rate	Discharge capacity (mAh g^{-1})/cycle no.	Ref.
Solid-state reaction	20	283/25	[14]
Precipitation	1 C	190/100	[20]
Solid-state reaction	20	116/50	[21]
Hydrothermal	100	200/100	[22]
Aerosol-assisted	400	150/5	[25]
Hydrothermal	100	350/100	[31]
Solid-state reaction	20	143/50	[42]
Sol-gel	4000	52/1000	[43]
Sol-gel	30 C	160/60	[44]

in case of a constant current density of 100 mA g^{-1} (Fig. 5b), the capacity loss between cycle 41 and 10 is even larger (e.g., Li_3VO_4-E(G) 10%). This observation can be also traced back to higher degradation effects of a more comprehensive de−/lithiation process as it is in the case of lower cycling rates [21]. Table 1 illustrates the electrochemical performance of Li_3VO_4 prepared via different synthesis methods. It is obvious that the electrochemical performance of Li_3VO_4 mainly depends on morphological features as particle size and surface texture. These parameters determine the specific surface of the material which is related to the transport path lengths.

Conclusions

In conclusion, a facile and low-cost approach was developed for the synthesis of Li_3VO_4 with different morphology by means of the hydrothermal microwave-assisted method. In particular, using a mixture of water and ethanol used as solvent yields hierarchically structured Li_3VO_4 microspheres assembled from stacked nanoflakes, while without ethanol, the procedure yields a rather bulk-like material with micro-sized primary particles. The electrochemical performance of the produced materials highlights the relevance of hierarchical structure and morphology for application in LIB. In comparison with the Li_3VO_4 bulk material, the hierarchical sphere-like particles show enhanced cycling performance which is associated with porous structure and large reaction area for the de−/insertion of Li-ions. The electrochemical activity is further boosted by grinding of the microspheres which significantly breaks the hierarchical structure while in general maintaining the size of the primary nanoparticles. The grinded material features a significantly improved specific capacity of 163 mAh g^{-1} which is straightforwardly explained by short Li-ion diffusion length and large surface area enabling good electronically conductive network by additives. Boosted capacity is however associated with lower cycling stability of the grinded nanocrystals which most presumingly is caused by the huge charge depth that leads to more pronounced degradation effects. In view of further optimization, a promising approach to suppress the pulverization upon cycling may be coating of the surface with carbon.

Acknowledgments The authors thank I. Glass for experimental support.

Funding information This work was supported by the Deutsche Forschungsgemeinschaft through project KL 1824/14-1. G.Z. acknowledges support of the state order via the Ministry of Science and High Education of Russia. E.T. acknowledges support by the BMWi through project 03ET6095C (HiKoMat).

References

1. Zhao B, Ran R, Liu M, Shao Z (2015) Mater Sci Eng R 98:1–71
2. Aravindan V, Lee Y-S, Madhavi S (2015) Adv Energy Mater 5(13): 1402225
3. Liu Y, Yang Y (2016) J Nanomater 2016:8123652
4. Croguennec L, Palacin MR (2015) J Am Chem Soc 137(9):3140–3156
5. Eftekhari A (2017) Energy Storage Mater 7:157–180
6. Xu Y, Wang L, Jia W, Yu Y, Zhang R, Li T, Fu X, Niu X, Li J, Kang Y (2019) Electrochim Acta 301:251–257
7. Zhu G-N, Wang Y-G, Xia Y-Y (2012) Energy Environ Sci 5(5): 6652–6667
8. Wang L, Wang F, Zhu J, Zhang X, Tang Y, Wang X (2018) Ceram Int 44(2):1296–1303
9. Chen Z, Belharouak I, Sun Y-K, Amine K (2013) Adv Funct Mater 23(8):959–969
10. Song T, Paik U (2016) J Mater Chem A 4(1):14–31
11. Wang Z, Zhang F, Xing H, Gu M, An J, Zhai B, Ana Q, Yu C, Li G (2017) Electrochim Acta 243:112–118
12. Xu J, Jia C, Cao B, Zhang WF (2007) Electrochim Acta 52(28): 8044–8047
13. Mo J, Zhang X, Liu J, Yu J, Wang Z, Liu Z, Yuan X, Zhou C, Li R, Wu X, Wu Y (2017) Chin J Chem 35(12):1789–1796
14. Li H, Liu X, Zhai T, Li D, Zhou H (2013) Adv Energy Mater 3(4): 428–432
15. Ni S, Zhang J, Ma J, Yang X, Zhang L, Li X, Zeng H (2016) Adv Mater Interfaces 3(1):1500340

16. Wang F, Liu Z, Yuan X, Mo J, Li C, Fu L, Zhu Y, Wu X, Wu Y (2017) J Mater Chem A 5(28):14922–14929
17. Li Q, Wei Q, Sheng J, Yan M, Zhou L, Luo W, Sun R, Mai L (2015) Adv Sci 2(12):1500284
18. Shen L, Chen S, Maier J, Yu Y (2017) Adv Mater 29(33):1701571
19. Shi Y, Wang J-Z, Chou S-L, Wexler D, Li H-J, Ozawa K, Liu H-K, Wu Y-P (2013) Nano Lett 13(10):4715–4720
20. Kim W-T, Jeong YU, Lee YJ, Kim YJ, Song JH (2013) J Power Sources 244:557–560
21. Liao C, Wen Y, Shan B, Zhai T, Li H (2017) J Power Sources 348: 48–56
22. Yang G, Zhang B, Feng J, Lu Y, Wang Z, Aravindan V, Aravind M, Liu J, Srinivasan M, Shen Z, Huang Y (2018) J Mater Chem A 6: 456–463
23. Ni S, Lv X, Ma J, Yang X, Zhang L (2014) J Power Sources 248: 122–129
24. Shi Y, Gao J, Abruña HD, Li H-J, Liu H-K, Wexler D, Wang J-Z, Wu Y (2014) Chem Eur J 20(19):5608–5612
25. Tartaj P, Amarilla JM, Vazquez-Santos MB (2016) Chem Mater 28(3):986–993
26. Song X, Jia M, Chen R (2002) J Mater Process Technol 120(1-3): 21–25
27. Du C, Wu J, Liu J, Yang M, Xu Q, Tang Z, Zhang X (2015) Electrochim Acta 152:473–479
28. Li Q, Wei Q, Wang Q, Luo W, An Q, Xu Y, Niu C, Tang C, Mai L (2015) J Mater Chem A 3(37):18839–18842
29. Zakharova GS, Ottmann A, Ehrstein B, Klingeler R (2016) Mater Res Bull 83:225–229
30. Ottmann A, Zakharova GS, Ehrstein B, Klingeler R (2015) Electrochim Acta 174:682–687
31. Yang G, Feng J, Zhang B, Aravindan V, Peng D, Cao X, Yu H, Madhavi S, Huang Y (2017) Int J Hydrog Energy 42(34):22167–22174
32. Xu L, Hu Y-L, Pelligra C, Chen C-H, Jin L, Huang H, Sithambaram S, Aindow M, Joesten R, Suib SL (2009) Chem Mater 21(13): 2875–2885
33. Lide DR (2004-2005) Handbook of chemistry and physics. CRC Press, New York
34. Chen H-I, Chang H-Y (2004) Colloids Surf A Physicochem Eng Asp 242(1-3):61–69
35. Ostwald W (1900) Z Phys Chem 34:495–503
36. Biswas S, Kar S, Chaudhuri S (2007) Mater Sci Eng B 142(2-3): 69–77
37. Sing KSW, Everett DH, Haul RAW, Moscou L, Pierotti RA, Rouquerol J, Siemieniewska T (1985) Pure App Chem:603–619
38. Sun P, Wang W, Liu Y, Sun Y, Ma J, Lu G (2012) Sensors Actuators B 173:52–57
39. Zhou L, Shen S, Peng X, Wu L, Wang Q, Shen C, Tu T, Huang L, Li J, Sun S (2016) ACS Appl Mater Interfaces 8(36):23739–23745
40. Iwama E, Kawabata N, Nishio N, Kisu K, Miyamoto J, Naoi W, Rozier P, Simon P, Naoi K (2016) ACS Nano 10(5):5398–5404
41. Ottmann A, Scholz M, Haft M, Thauer E, Schneider P, Gellesch M, Nowka C, Wurmehl S, Hampel S, Klingeler R (2017) Sci Rep 7: 23914
42. Shao G, Gan L, Ma Y, Li H, Zhai T (2015) J Mater A 3:11253–11260
43. Zhang C, Liu C, Nan X, Song H, Liu Y, Zhang C, Cao G (2016) ACS Appl Mater Interfaces 8(1):680–688
44. Liu J, Lu P-J, Liang S, Liu J, Wang W, Lei M, Tang S, Yang Q (2015) Nano Energy 12:709–724